Eurographics/ ACM SIGGRAPH Symposium on Computer Animation (2007)
D. Metaxas and J. Popovic (Editors)

Cubic Shells

Akash Garg
Columbia University, USA

Eitan Grinspun
Columbia University, USA

Max Wardetzky
Freie Universität Berlin, Germany

Denis Zorin
New York University, USA

Abstract

Hinge-based bending models are widely used in the physically-based animation of cloth, thin plates and shells. We propose a hinge-based model that is simpler to implement, more efficient to compute, and offers a greater number of effective material parameters than existing models. Our formulation builds on two mathematical observations: (a) the bending energy of curved flexible surfaces can be expressed as a cubic polynomial *if the surface does not stretch; (b) a general class of anisotropic materials—those that are* orthotropic*—is captured by appropriate choice of a single stiffness per hinge. Our contribution impacts a general range of surface animation applications, from isotropic cloth and thin plates to orthotropic fracturing thin shells.*

1. Introduction

Many animation applications require simple and efficient simulation of a general class of elastic surfaces. This class includes objects that are (a) flat (plates) or curved (shells) in their undeformed state, (b) flexible or nearly rigid and (c) isotropic or anisotropic in their response to bending. In mesh-based simulation, *hinge-based* methods are preferred for their simplicity and economy of computation. Considering every two triangles meeting at an edge to be a bending hinge, such methods require that some function of the dihedral angle is subject to a restoring force. Empirically, hinge-based models are known to work well for isotropic materials, and for geometric models of anisotropy based on Euler's curvature formula [BW98, VMT06]. For a survey of bending models used in animation, see [TW06].

Contributions. We present what we believe is the simplest and most efficient hinge-based bending model to encompass the spectrums (a), (b), and (c), at the cost of restricting our attention to *quasi-inextensible* surfaces, *i.e.*, surfaces that prefer to bend much more than to stretch. Our model is based on a mathematical analysis of the hinge-based approach resulting in two main insights:

First, we introduce a hinge-based bending model that preserves a key property of the smooth setting: the bending energy of a thin shell is *cubic* under isometric deformations. To understand the consequences of this statement, consider that bending energy is in general a highly nonlinear functional of the surface position; therefore, the implementation of implicit solvers for thin shells involves relatively complex derivation and costly computation of the nonlinear bending force Jacobian. However, under the assumption of quasi-isometry, we show that implementation can be reduced to a one-time precomputation of an approximate Jacobian matrix, and implicit time stepping routines can use an inexact Newton method for significant performance gains. Shells simulated with this method conserve both linear and angular momenta.

Second, we treat anisotropy, where mechanical response depends on the direction of applied strain. We present a bending model for *orthotropic* materials, exposing an important physical parameter—the *shear modulus*—which affects the *drapability* of a fabric [SM02]. Perhaps due to their small stencil, hinge-based models in computer animation have thus far eluded the incorporation of orthotropic response.

Our work builds on a foundation laid out by Bergou *et al.* [BWH*06], who demonstrated that in the special case of isotropic thin *plates* undergoing isometric deformations, the bending energy is quadratic, and correspondingly the forces are linear, in mesh positions; see also Volino and Magnenat-Thalmann [VMT06] for a linear bending force. In contrast, we consider inextensible thin *shells*, whose bending energy is cubic, with correspondingly quadratic forces.

Overview. By first considering *isotropic* bending, we expose the cubic nature of bending energies in the smooth (§2.1) as well as discrete settings (§2.2), establishing the *cubic hinge* (§3) as our discrete building block. Next, we introduce *orthotropy* (§4) and show that it is captured by a scalar hinge stiffness (§4.1). Finally, we describe the efficient implementation of orthotropic cubic shells (§5–§6), and discuss a battery of experiments demonstrating the efficiency and efficacy of our model (§7–§8).

Copyright © 2007 by the Association for Computing Machinery, Inc.
Permission to make digital or hard copies of part or all of this work for personal or classroom use is granted without fee provided that copies are not made or distributed for commercial advantage and that copies bear this notice and the full citation on the first page. Copyrights for components of this work owned by others than ACM must be honored. Abstracting with credit is permitted. To copy otherwise, to republish, to post on servers, or to redistribute to lists, requires prior specific permission and/or a fee. Request permissions from Permissions Dept, ACM Inc., fax +1 (212) 869-0481 or e-mail permissions@acm.org.
SCA 2007, San Diego, California, August 04 - 05, 2007
© 2007 ACM 978-1-59593-624-4/07/0008 $ 5.00

2. Isotropic bending

2.1. Smooth setting

Consider a surface deformed away from its natural (*undeformed*) shape. To this deformation we associate the isotropic bending energy

$$E_{\mathrm{b}}(\mathbf{x}) = \frac{1}{2}\int_S (H-\overline{H})^2 \mathrm{d}A\,. \tag{1}$$

This is the integral, over the undeformed surface, of the squared change in mean curvature. Here $\mathbf{x}$ is the position of the deformed surface, and H is the mean curvature function of the deformed surface. A bar (*e.g.*, $\overline{H}$) denotes the corresponding quantity evaluated on the undeformed surface. Whereas we consider arbitrary undeformed shapes, the special case of flat undeformed shapes ($\overline{H}=0$) was explored by Bergou *et al.* [BWH*06].

Although not immediately apparent from (1), $E_{\mathrm{b}}(\mathbf{x})$ is actually a *cubic polynomial* in $\mathbf{x}$ under *isometric deformations*, *i.e.*, if the surface is allowed to bend but not to stretch. To see this, rewrite (1) as

$$E_{\mathrm{b}}(\mathbf{x}) = \frac{1}{2}\int_S \left(\langle \mathbf{H},\mathbf{H}\rangle - 2\langle \mathbf{H},\overline{H}\hat{\mathbf{n}}\rangle + \overline{H}^2\right)\mathrm{d}A\,. \tag{2}$$

Here $\langle\cdot,\cdot\rangle$ denotes the standard inner product in 3-space, and $\mathbf{H}=H\hat{\mathbf{n}}$ stands for the mean curvature *normal*, a vector parallel to the surface's unit normal, $\hat{\mathbf{n}}$. Bergou *et al.* observed that the mean curvature vector can be expressed as $\mathbf{H}=\Delta\mathbf{x}$, *i.e.*, the surface's intrinsic Laplacian applied to the position of the surface. For isometric deformations of the surface, two facts follow: (F1) Since Δ is intrinsic, $\mathbf{H}$ is *linear in surface position*, thus $\langle\mathbf{H},\mathbf{H}\rangle$ is quadratic in $\mathbf{x}$ [BWH*06]. (F2) The surface normal is quadratic† in $\mathbf{x}$; therefore, $\langle\mathbf{H},\overline{H}\hat{\mathbf{n}}\rangle$ is cubic. It follows that $E_{\mathrm{b}}(\mathbf{x})$ is a cubic polynomial in $\mathbf{x}$, because $\langle\mathbf{H},\overline{H}\hat{\mathbf{n}}\rangle$ is cubic, $\langle\mathbf{H},\mathbf{H}\rangle$ is quadratic, and $\overline{H}^2$ does not depend on $\mathbf{x}$. While Bergou *et al.* discussed (F1) for thin plates ($\overline{H}=0$), (F2) is unique to shells ($\overline{H}\neq 0$) and presents our central technical challenge.

The *cubic shells* idea is to develop a discrete analogue of this picture.

2.2. Discrete setting

Consider a triangle mesh whose shape before deformation is given by the vector of vertex positions $\bar{\mathbf{x}}$. When the mesh is deformed to position $\mathbf{x}$, the usual hinge-based bending energy [BW98, BMF03, GHDS03, BWH*06, TW06] is given

† To see that $\hat{\mathbf{n}}$ is quadratic, write $\hat{\mathbf{n}} = \frac{\partial\mathbf{x}}{\partial u}\times\frac{\partial\mathbf{x}}{\partial v}$, and observe that orthonormality of tangent vectors, $\frac{\partial\mathbf{x}}{\partial u}$ and $\frac{\partial\mathbf{x}}{\partial v}$, is preserved under isometric deformations.

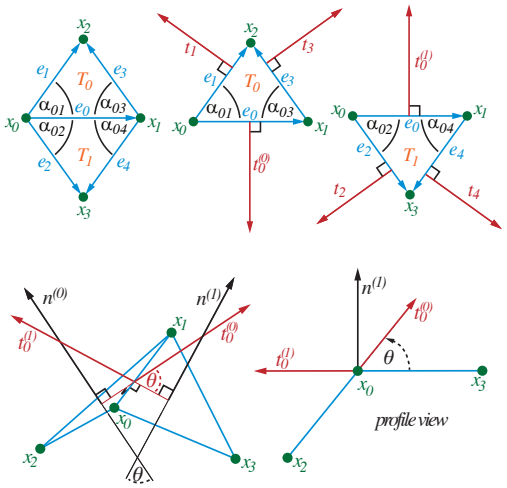

Figure 1: Top-left: *Hinge stencil for an interior edge.* Top-middle and -right: *Perpendicular vectors used in the computation.* Bottom: *Hinge in 3-space with corresponding labels.*

by‡

$$E_{\mathrm{b}}(\mathbf{x}) = \frac{1}{2}\sum_i \frac{3|\bar{\mathbf{e}}_i|^2}{\overline{A}_i}\left(2\sin\frac{\theta_i-\bar{\theta}_i}{2}\right)^2\,. \tag{3}$$

Here the sum is taken over all interior edges, $\overline{A}_i$ denotes the combined area of the two triangles incident to edge $\bar{\mathbf{e}}_i$, and θ_i denotes the dihedral angle at edge i.

Our goal is to establish an important, and previously overlooked, property of (3): under isometric deformations, it is a cubic polynomial in $\mathbf{x}$. This observation will expose a much more efficient implementation than is directly evident from (3); for details on this implementation, refer directly to §5.

The discrete energy (3) can be written as a sum over contributions from every hinge (indexed by i). Using the identity $2\sin^2 u = 1-\cos 2u$, with $u=(\theta-\bar{\theta})/2$, we arrive at an expression of energy associated to the i^{th} hinge:

$$E_{\mathrm{b}}(\mathbf{x})_i = \frac{3|\bar{\mathbf{e}}_i|^2}{\overline{A}_i}(1-\cos(\theta_i-\bar{\theta}_i))\,. \tag{4}$$

In the following section, we prove that for isometric deformations this hinge energy is cubic in $\mathbf{x}$.

3. The cubic hinge

Our derivation uses the geometric construction in Figure 1, which defines *local indices* of the triangles, $\{T_0,T_1\}$, edge vectors, $\{\mathbf{e}_0,\ldots,\mathbf{e}_4\}$, and vertex positions, $\{\mathbf{x}_0,\ldots,\mathbf{x}_3\}$, associated to a hinge. Note the construction of *perpendiculars* $\mathbf{t}_i$: each edge vector $\mathbf{e}_i$ is rotated 90 degrees, on the

‡ For planar rest state ($\bar{\theta}=0$) we have $\lim_{\theta\to 0} 2\sin\theta/2 = \lim_{\theta\to 0} 2\tan\theta/2 = \theta$, so that models that use $2\sin\theta/2$, $2\tan\theta/2$, or θ coincide in the limit of an appropriate refinement sequence.

© Association for Computing Machinery, Inc. 2007.

plane of the triangle, to point outwards (thus $|\mathbf{t}_i| = |\mathbf{e}_i|$ and $\langle \mathbf{t}_i, \mathbf{e}_i \rangle = 0$). Since $\mathbf{e}_0$ is associated to two triangles, we construct two perpendiculars, $\mathbf{t}_0^{(0)}$ and $\mathbf{t}_0^{(1)}$, on the planes of triangles T_0 and T_1 respectively.

Expressing the perpendiculars $\mathbf{t}_0^{(0)}$ (resp. $\mathbf{t}_0^{(1)}$) in the edge basis $\{\mathbf{e}_1, \mathbf{e}_3\}$ (resp. $\{\mathbf{e}_2, \mathbf{e}_4\}$) we obtain

$$\mathbf{t}_0^{(0)} = -\cot\alpha_{03}\mathbf{e}_1 - \cot\alpha_{01}\mathbf{e}_3 \,, \tag{5}$$

$$\mathbf{t}_0^{(1)} = -\cot\alpha_{04}\mathbf{e}_2 - \cot\alpha_{02}\mathbf{e}_4 \,. \tag{6}$$

Under isometric deformation, interior angles remain constant, therefore $\mathbf{t}_0^{(0)}$ and $\mathbf{t}_0^{(1)}$ are *linear expressions* in the position of the mesh. Furthermore, the geometry of Fig. 1-bottom reveals that[§]

$$\cos\theta = \frac{-\langle \mathbf{t}_0^{(0)}, \mathbf{t}_0^{(1)} \rangle}{|\mathbf{e}_0|^2}, \quad \text{and} \quad \sin\theta = -\frac{\beta[\mathbf{e}_0, \mathbf{e}_1, \mathbf{e}_2]}{|\mathbf{e}_0|^2} \,,$$

where $[\mathbf{e}_i, \mathbf{e}_j, \mathbf{e}_k]$ is the scalar triple product $(\mathbf{e}_i \times \mathbf{e}_j) \cdot \mathbf{e}_k$, and $\beta = \frac{1}{|\mathbf{e}_0|}(\cot\alpha_{01} + \cot\alpha_{03})(\cot\alpha_{02} + \cot\alpha_{04})$.

Expanding (4) by the identity $\cos(\theta - \bar{\theta}) = \cos\theta\cos\bar{\theta} + \sin\theta\sin\bar{\theta}$, substituting the above expressions for $\cos\theta$ and $\sin\theta$, and simplifying the resulting expression by using the isometry assumption ($|\bar{\mathbf{e}}_i| = |\mathbf{e}_i|$) we find that (4) equals

$$\underbrace{\frac{3}{\bar{A}_0}\left(|\bar{\mathbf{e}}_0|^2 + \langle \mathbf{t}_0^{(0)}, \mathbf{t}_0^{(1)} \rangle \cos\bar{\theta}\right)}_{\text{thin plate component}} + \underbrace{\frac{3\bar{\beta}}{\bar{A}_0}[\mathbf{e}_0, \mathbf{e}_1, \mathbf{e}_2]\sin\bar{\theta}}_{\text{cubic term}} \,. \tag{7}$$

Under isometry, the energy associated to an individual hinge is a cubic polynomial in $\mathbf{x}$. Just as in the smooth picture, the discrete $E_b(\mathbf{x})$ is cubic. Note that for the special case $\bar{\theta} = 0$, we recover the quadratic bending thin *plate* energy of [BWH*06] simply by substituting (5) and (6) into (7).

4. Orthotropy

We now generalize our bending model to *orthotropic* materials—an important class of anisotropic materials whose elastic properties depend on the direction along which they are measured [VK01]. A fully general linear elasticity model for deformable surfaces has six parameters (not counting the choice of anisotropy axes) some of which are hard to interpret intuitively. We focus on a more restricted *orthotropic* elasticity model whose four parameters have more intuitive meaning and appear to be useful for material behavior control in animation. Most common man-made materials are orthotropic, for example, cloth, plastic reinforced by fibers, sheet metal, and paper. Non-orthotropic thin materials are less common (*e.g.*, thin sheets obtained by cutting a 3D orthotropic material at an angle, or composite materials). For cloth, orthotropic approximation naturally matches most of the parameters of the Kawabata cloth evaluation system [Kaw80], a commonly used system for characterizing cloth properties, as explained below.

We are primarily interested in how these material parameters affect *bending*, rather than in-plane deformations. From the four parameters of orthotropic materials, one parameter can be eliminated if we assume that bending the surface along material directions does not have any effect on bending on the other direction (this corresponds to having zero Poisson ratio in the isotropic case). For simplicity we will assume that this is the case, and briefly discuss the role of the Poisson ratio at the end of this section.

The most obvious of the remaining three parameters are two Young's moduli, Y^0 and Y^1, which determine bending stiffness along two material directions. The third parameter is the *shear modulus*, G^{01}, which, for in-plane deformations, determines the resistance to shear. In the case of bending, the shear modulus allows for additional directional variability of bending stiffness. Specifically, bending stiffness at an angle α with respect to the material axis 0, is given by (up to a scale factor):

$$Y^0\cos^4\alpha + Y^1\sin^4\alpha + 2G^{01}\sin^2\alpha\cos^2\alpha \,. \tag{8}$$

Consider the adjacent plot of *directional stiffness* as a function of α, for three materials all sharing $Y^0 = Y^1$, but with shear moduli $0.1K$, K, and $2K$. Note that for low shear, typical for cloth, the maximal to minimal bending stiffness ratio is 2. As shown in Figure 4, this has a significant effect on drapability, and *cannot* be achieved by a simple model using just two parameters. Similarly, the shear modulus affects resistance of cloth to *twisting*, even if $Y^0 = Y^1$, as twisting may lead to diagonal bending.

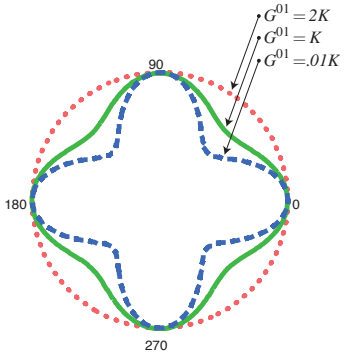

Directional stiffness is particularly important in the case of *quasi-inextensible* flat sheets. Such sheets have small Gaussian curvature (the product of the two principal curvatures), which implies that strong bending can be present only in a single direction.

In contrast to directional stiffness, forces arising from the interaction of *multiple* bending directions (*e.g.*, due to the Poisson ratio in the isotropic case) appear to be qualitatively less important. In fact, one can show that for directional stiffness this interaction results in effective increase in the shear

[§] The expression for $\sin\theta$ was derived from

$$\sin\theta = \frac{\langle \mathbf{t}_0^{(0)}, \mathbf{n}^{(1)} \rangle}{|\mathbf{e}_0|^2} = -\frac{[\mathbf{t}_0^{(0)}, \mathbf{t}_0^{(1)}, \mathbf{e}_0]}{|\mathbf{e}_0|^3} = -\frac{\beta[\mathbf{e}_0, \mathbf{e}_1, \mathbf{e}_2]}{|\mathbf{e}_0|^2} \,,$$

where $\mathbf{n}^{(1)} = (|\mathbf{e}_0|/|\mathbf{e}_4 \times \mathbf{e}_2|)\mathbf{e}_4 \times \mathbf{e}_2$ is a scaled triangle normal. The last step is obtained by using (5) and (6) to replace $\mathbf{t}_0^{(0)}$ and $\mathbf{t}_0^{(1)}$, followed by observing that $\mathbf{e}_4 = \mathbf{e}_2 - \mathbf{e}_0$ and $\mathbf{e}_3 = \mathbf{e}_1 - \mathbf{e}_0$.

© Association for Computing Machinery, Inc. 2007.

modulus. One can prove that in the simple case of bending of a plate with fixed boundaries the bending forces (unlike stretching) are independent of the Poisson ratio.

The Kawabata system characterizes cloth by its resistance to bending along warp and along weft directions, and by tensile, shearing and compressive stiffnesses measured as functions of deformation. In the orthotropic elasticity model, stiffnesses are assumed to be independent of the deformation, which appears to be a good approximation for qualitative modeling. Furthermore, plasticity effects are ignored, and the compressive and tensile stiffnesses are assumed to be equal. As pointed out in [BD94], linear elasticity provides a good approximation for Kawabata measurements for small deformations, although it ignores some of the subtler initial-resistance effects.

Given Kawabata measurements of a fabric, Y^1 and Y^0 can be inferred from directional bending stiffnesses and tensile measurements, and G^{01} from shear measurements. Alternatively, Y^1, Y^0, G^{01}, and the material axes may be directly controlled by an artist, adjusting parameters based on the notion that Y^1 and Y^0 determine resistance to bending along the two orthogonal material directions and G^{01} determines the resistance of the material to draping over an object.

Given the material parameters, and applying a standard formulation of Hooke's law for orthotropic materials, we can express the bending energy density of a deformed surface as a function of bending strain ε, using one additional material parameter $Y^{01} = \nu_{01}Y^1 = \nu_{10}Y^0$, where ν_{10} and ν_{01} are Poisson ratios (which always satisfy $\nu^{01}/Y^0 = \nu^{10}/Y^1$). The energy density is

$$c\left(Y^0\varepsilon_{00}^2 + Y^1\varepsilon_{11}^2 + 2Y^{01}\varepsilon_{00}\varepsilon_{11}\right) + 2hG^{01}\varepsilon_{01}^2\,, \qquad (9)$$

where $c = hY^0Y^1/(Y^0Y^1 - Y^{01}Y^{01})$, $h = \tau^3/12$, and τ is the sheet thickness. The bending strain is the shape operator [dC92] for surface, which for a quadratic bending energy reduces to the matrix of second partial derivatives. For the special case of isotropic materials, $Y^0 = Y^1 = 2(1+\nu)G^{01} = Y^{01}/\nu$.

In the following section, we show that orthotropic effects can be captured by weighting each hinge stiffness by a scalar factor, $\bar{\lambda}_i$. For convenience of implementation, the results of this derivation are summarized in §5.1.

4.1. Derivation of hinge stencil orthotropy

In §2.2 we discussed a simple model of discrete bending energy for isotropic shells. We based this model on summing the contributions of squared mean curvatures over interior edges. While discrete mean curvatures suffice to cover the isotropic case, we must use a discretization of the full shape operator in the anisotropic case. Indeed, smooth anisotropic energy density (9) requires expressing the discrete shape operator as a symmetric 2×2 matrix in the material frame—as the entries of this matrix measure bending and shearing stiffness in principal material directions. A hinge-based discrete shape operator $\mathbf{S}$ has been successfully applied in geometric modeling [HP04]. Here we augment the geometric modeling view by two aspects: (a) we express $\mathbf{S}$ in a material frame as opposed to its original expression in a principal curvature frame, and (b) we show how $\mathbf{S}$ leads to a scalar stiffness-correcting factor per edge covering the discrete orthotropic case.

Let us briefly recall the geometric view based on discrete principal curvatures taken in [HP04]. It is well-known from the smooth case [dC92] that $\mathbf{S}$ corresponds to a quadratic form whose (orthogonal) eigenvectors correspond to the two principal curvature directions, and its eigenvalues correspond to the principal curvatures, κ_0 and κ_1. Recall also that mean curvature is given as $H = \kappa_0 + \kappa_1$. In the discrete *edge-based* view, [HP04] defines the two principal curvature directions as (1) the direction along the edge and (2) the direction perpendicular to the edge—with no curvature ($\kappa_0 = 0$) along the edge and normal curvature ($\kappa_1 = \kappa$) perpendicular to the edge. Consequently, $H = \kappa$, and in the edge-based principal curvature frame, the discrete shape operator takes the form

$$\mathbf{S} = \begin{pmatrix} 0 & 0 \\ 0 & \kappa \end{pmatrix} = H \begin{pmatrix} 0 & 0 \\ 0 & 1 \end{pmatrix}\,.$$

We note that this hinge-based shape operator is mesh dependent (in particular, principal directions are tied to edge directions). However, if the edge directions are distributed evenly, on the average the true shape operator is well approximated.

In order to express $\mathbf{S}$ in the material frame, we treat the mesh area associated with each hinge stencil as a *homogeneous* piece of material, *i.e.*, we assume that the material parameters cY^0, cY^1, cY^{01}, hG^{01}, and the material axes are *constant* over hinge stencils. Denoting by γ_0 the angle between edge $\mathbf{e}_i$ and the first material axis, $\hat{\mathbf{y}}_a$, and using the fact that the shape operator transforms like a quadratic form, we obtain that $\mathbf{S}$ takes the form

$$\mathbf{S}_i = H_i \begin{pmatrix} \sin^2\gamma_0 & -\sin\gamma_0\cos\gamma_0 \\ -\sin\gamma_0\cos\gamma_0 & \cos^2\gamma_0 \end{pmatrix}\,,$$

when expressed in the material frame of the edge i. Finally, using the smooth energy density (9) and setting $\varepsilon = \mathbf{S}$, it follows from basic trigonometric identities that the discrete orthotropic density can be written as

$$\underbrace{\left((cY^0)\sin^4\gamma_0 + (cY^1)\cos^4\gamma_0 + \frac{1}{2}\left(cY^{01} + hG^{01}\right)\sin^2(2\gamma_0)\right)}_{\bar{\lambda}_i} \cdot H_i^2\,,$$

providing a way to adjust hinge weights to effect orthotropic response.

This completes the requisite derivations for orthotropic cubic shells. In the following, we discuss the implementation of our model (§5–§6) and demonstrate the generality of the model with various simulation examples (§7).

© Association for Computing Machinery, Inc. 2007.

5. Implementing cubic shells

In this section we describe the computation of forces and force Jacobians for the cubic shells energy, (7). Consider a mesh with n vertices and coordinate vectors $\mathbf{x}^x, \mathbf{x}^y, \mathbf{x}^z \in \mathbb{R}^n$. *Hinge-centric* computations are expressed in terms of the hinge's *local indices* (Fig. 1) for triangles, $\{T_0, T_1\}$, edge vectors, $\{\mathbf{e}_0, \ldots, \mathbf{e}_4\}$, and vertex positions, $\{\mathbf{x}_0, \ldots, \mathbf{x}_3\}$.

Precomputation. Recall that quantities that depend only on the undeformed positions are decorated with a bar, *e.g.*, $\bar{\mathbf{x}}$. Compute barred quantities once, before the simulation.

One-time matrix assembly. Assemble the global $n \times n$ matrix, $\overline{\mathbf{Q}}$, by iterating over hinge stencils. In the usual style of *stiffness matrix assembly* [ZT89], $\overline{\mathbf{Q}}$ accumulates contributions from each *local* 4×4 matrix, $\overline{\mathbf{Q}}_i$:

$$\overline{\mathbf{Q}}_i = \left(\frac{3\overline{\lambda}_i \cos\overline{\theta}_i}{\overline{A}_i} \right) \overline{K}_i^T \, \overline{K}_i \, ,$$

where $\overline{\lambda}_i$ is the stiffness of the hinge, $\overline{A}_i$ is the combined area of the two hinge triangles, and $\overline{\theta}_i$ is the undeformed hinge angle. In local indices, $\cos\overline{\theta} = -\langle \bar{\mathbf{t}}_0^{(0)}, \bar{\mathbf{t}}_0^{(1)} \rangle / |\bar{\mathbf{e}}_0|^2$, and $\overline{K} = (\overline{c}_{03} + \overline{c}_{04}, \overline{c}_{01} + \overline{c}_{02}, -\overline{c}_{01} - \overline{c}_{03}, -\overline{c}_{02} - \overline{c}_{04}) \in \mathbb{R}^4$, where $\overline{c}_{jk} = \cot \angle \bar{\mathbf{e}}_j, \bar{\mathbf{e}}_k$.

Force computation. Compute forces by adding thin plate and nonflat contributions. Compute thin plate contributions globally as the matrix-vector products $\mathbf{f}^x = \overline{\mathbf{Q}}\mathbf{x}^x$, $\mathbf{f}^y = \overline{\mathbf{Q}}\mathbf{x}^y$, $\mathbf{f}^z = \overline{\mathbf{Q}}\mathbf{x}^z$. Compute nonflat contributions by accumulating local hinge contributions

$$\begin{aligned} \mathbf{f}_0 &= -\mathbf{f}_1 - \mathbf{f}_2 - \mathbf{f}_3 \, , & \mathbf{f}_1 &= \overline{k}(\mathbf{e}_1 \times \mathbf{e}_2) \, , \\ \mathbf{f}_2 &= \overline{k}(\mathbf{e}_2 \times \mathbf{e}_0) \, , & \mathbf{f}_3 &= \overline{k}(\mathbf{e}_0 \times \mathbf{e}_1) \, , \end{aligned}$$

where $\overline{k} = 3\overline{\lambda}_i(\overline{c}_{01} - \overline{c}_{03})(\overline{c}_{04} - \overline{c}_{02})[\bar{\mathbf{e}}_0, \bar{\mathbf{e}}_1, \bar{\mathbf{e}}_2] / (\overline{A}_0 |\bar{\mathbf{e}}_0|^3)$.

Force Jacobian computation. The exact force Jacobian ($\mathbb{R}^{3n} \times \mathbb{R}^{3n}$) is obtained by adding the thin plate and the nonflat contributions. The thin plate contributions are given by $\partial \mathbf{f}^x / \partial \mathbf{x}^x = \partial \mathbf{f}^y / \partial \mathbf{x}^y = \partial \mathbf{f}^z / \partial \mathbf{x}^z = \overline{\mathbf{Q}}$. For best performance (without sacrifice of accuracy), the nonflat contribution is omitted (as explained in §6); for completeness of exposition the nonflat contribution is detailed in the Appendix A.

5.1. Orthotropic hinge

The simple expressions above are all that is required to implement a cubic hinge-based bending force, given a stiffness value $\overline{\lambda}_i$ per hinge. For homogeneous isotropic materials, $\overline{\lambda}_i = \overline{\lambda}$ does not vary over the mesh, and the above derivation suffices; if a general class of orthotropic materials is desired, then $\overline{\lambda}_i$ should be computed by the formula derived in (§4.1); recall $\overline{\lambda}_i =$

$$(cY^0)\sin^4\gamma_0 + (cY^1)\cos^4\gamma_0 + \frac{1}{2}\left(cY^{01} + hG^{01}\right)\sin^2(2\gamma_0) \, ,$$

where γ_0 is the angle between the hinge edge and the first material axis, $\hat{\mathbf{y}}_0$, and Y^0, Y^1, Y^{01}, and G^{01} are the material parameters described above. The above expression is all that is needed to implement orthotropic bending for cubic shells, and indeed for any existing hinge-based model.

In our implementation, the (spatially-varying) direction of $\hat{\mathbf{y}}_0$ is encoded by a coordinate function over a given parameterization of the surface. In particular, we use the color values of a texture map to encode the direction of the material axis.

6. Efficient simulation of thin shells

The separability of the force Jacobian of cubic shells into a constant and linear term opens several interesting possibilities for efficient time integration of thin shell dynamics. Among common discrete time-stepping schemes [Hau04, HLW06, BW98], implicit schemes are popular in animation due to their stability. Implicit schemes advance time by solving a (typically nonlinear) system of equations. The system is usually solved by repeated Newton iterations (although *semi-implicit* methods complete a single Newton iteration) [PTVF92]. Each Newton iteration requires an evaluation of the force, $-\nabla E$, as well as the force Jacobian.

The fixed points of Newton's method remain unaltered when the nonlinear system Jacobian is replaced by any invertible matrix. An inexact Newton's method [Mor99] uses this fact in replacing a costly Jacobian with an inexpensive approximant. Hauth [Hau04] used an approximation of the in-plane stretching force Jacobian, and an inexact Newton framework, to accelerate cloth simulations; our work is similar, but we approximate the bending Jacobian. Wardetzky *et al.* [WBH*] also used an inexact Newton solve, in a mesh smoothing application; in contrast to that application, we treat the dynamics of shells having nonflat undeformed configurations.

Experiment. We consider the application of the inexact Newton's method with approximations to the bending force Jacobian. To provide a standard and easily-reproducible point of reference, we consider the Euler method, fully-implicit on stretching and bending elastic forces, without any additional damping forces.

In our experiments we pair two possible bending forces with three possible force Jacobians. For the two forces we consider the *nonlinear hinge* (NH)—the force resulting from treating bending energy fully nonlinearly (*i.e.*, by dropping the isometry assumption)—and the *cubic shells force* (CS) arising from our cubic energy as discussed in the previous section. For the three force Jacobians we consider the *nonlinear hinge Jacobian* (NH), the *entire* cubic shells Jacobian (CS), and the *constant part* (CC) of the cubic shells Jacobian. A particular choice of (inexact) Newton is denoted by a 2-tuple, *e.g.*, (CS,CC) denotes the use of the cubic shell bending forces paired with an approximate constant Jacobian; (NH,NH) denotes the usual fully-implicit implementation of the nonlinear hinge.

As a baseline, we run (NH,NH) at the maximum stable step

© Association for Computing Machinery, Inc. 2007.

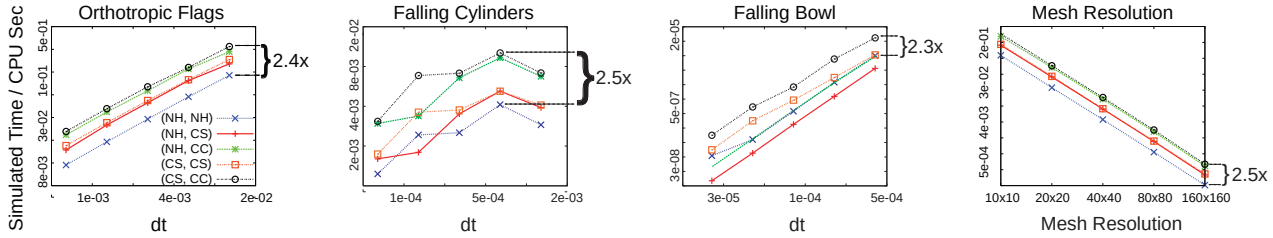

Figure 2: *(*Left:*) Performance measured in completed simulation time per CPU second (y-axes) as a function of discrete time step (x-axes). Higher values mean better performance. In an inexact Newton framework, Cubic Shells dominate performance for all tested scenarios, including (left-to-right) Orthotropic Flags (Fig. 5), Falling Cylinders (Fig. 3), and Falling Bowl (Fig. 7).* Right: *Performance as a function of mesh resolution (from* 10×10 *to* 160×160 *regular grids), demonstrating that the benefits of cubic shells are not resolution-dependent. Timing numbers include timestepping and collision detection/response.*

size, and four smaller step sizes; these step sizes are reused in runs of (NH, CS), (NH, CC), (CS, CS), (CS, CC). We measure performance of these runs for various problem scenarios (see §7 and video).

We record the performance of each method, measured as the ratio *completed simulation time per CPU second*, *i.e.*, higher values mean better performance (see Figure 2–left). The cubic shells with an approximate *constant* Jacobian, (CS,CC), dominates all methods for all problem scenarios. Note that the performance gains observed for (CS, CC) are independent of mesh resolution (see Figure 2–right).

7. Visual impact of orthotropic parameters

Orthotropic parameters provide additional artistic control over the dynamics of wrinkles and folds. Consider for example a flag tailored by cutting a rectangular pattern from an orthotropic textile. The orientation of warp and weft relative to the flag's pattern, as well as the values of Young's and shear moduli, have considerable visual impact on the resulting dynamics (see Fig. 5 and accompanying video).

The orthotropic shear modulus plays an important role in the *drapability* of a fabric [SM02]; the shear modulus is *not* captured by geometric models that employ Euler's formula, such as [BW98, VMT06], or elliptic interpolation, such as [CK03]. A high shear modulus tends to align folds and wrinkles to the material axes; a lower shear modulus allows the fabric to fold along other directions, and therefore to obtain a closer fit to the body. The first two frames of Fig. 4 compare a high and low shear modulus, respectively, illustrating the intuitive notion of drapability. When a high shear modulus is desired (leftmost frame), the Young's modulus is a poor substitute—it is unable to capture stiff extrusion of the poncho around the shoulders without introducing extraneous stiffness elsewhere.

Furthermore, orthotropy has a strong effect on the interaction between a material and its environment. We simulate the fall and bounce of four elastic cylinders, each with a different orientation for its principal material axis. The resulting animation (Fig. 3 and accompanying video) reveals the extreme variations in deformation and overall trajectory that arise purely from changing the orthotropic parameters.

Orthotropy indirectly enriches any other technologies implemented in the simulator, such as viscoelasticity or fracture [TF88]. For example, the anisotropic bending resulting from collisions produces distinctive fracture patterns both for plates (Fig. 6) and shells (Fig. 7). For a summary of the fracture algorithm refer to Appendix B.

8. Discussion

Limitations. The cubic hinge does not overcome those limitations that are shared by all hinge-based approaches. In particular, the simplicity of hinge-based models comes at the cost of limited convergence behavior and meshing-dependence [GGRZ06].

Implicit to the cubic hinge is the assumption that the surface deforms isometrically, *i.e.*, without stretching. A natural question, then, is how much stretching is permissible in practice, and what are the failure modes of the model under excessive stretching? To explore these questions, we resimulate the falling cylinder and falling bowl using progressively lower stretching resistance. Both examples remain well-behaved so long as the stretching stiffness is two orders of magnitude greater than the bending stiffness; during the simulation, the meshes stretch by as much as 15%.

If we reduce stretching stiffness even further, then for the thin *shell* examples we observe a slow, noticeable stretching of the surface, in particular, in an expanding (not oscillatory) mode. This is perhaps not surprising, since a cubic energy is not bounded from below; under normal (quasi-isometric) circumstances, the stretching resistance prevents this infinite well from being exploited.

We repeat the above experiment with the billowing flag. Since the flag has a flat undeformed configuration, the cubic energy term vanishes, leaving a quadratic energy bounded from below. We observe that the flag simulation is well-behaved even when strong wind induces stretching of 300%.

Conserved momenta. In all circumstances (even when parasitic stretching is observed due to a broken isometry assumption), the simulated model conserves linear and angular momenta. To see this, note that the quadratic forces arising

© Association for Computing Machinery, Inc. 2007.

from the cubic energy are *not* approximated (only their Jacobian is); since the cubic energy is invariant under rigid body transformations of the deformed (and also the undeformed) configuration, forces induced by this energy do not apply a global acceleration or torque.

Due to its simplicity, efficiency, and generality, we expect cubic shells to be of practical relevance in computer animation.

Acknowledgments We thank David Harmon for providing robust collision detection and response code. We thank David Eberle and the anonymous reviewers for their feedback. This work was supported in part by the DFG Research Center MATHEON in Berlin, the NSF (MSPA-IIS-05-28402, CSR-CNS-06-14770, CCR-0093390, CAREER-CCF-06-43268), Autodesk, Elsevier, mental images, NVIDIA, and an IBM Faculty Parternship award.

References

[BD94] BREEN D., DONALD H.: House, and Michael J. Wozny. Predicting the drape of woven cloth using interacting particles. *Proceedings of SIGGRAPH '94* (1994), 365–372.

[BMF03] BRIDSON R., MARINO S., FEDKIW R.: Simulation of clothing with folds and wrinkles. *SCA* (2003), 28–36.

[BW98] BARAFF D., WITKIN A.: Large steps in cloth simulation. In *SIGGRAPH* (1998), ACM Press, pp. 43–54.

[BWH*06] BERGOU M., WARDETZKY M., HARMON D., ZORIN D., GRINSPUN E.: A quadratic bending model for inextensible surfaces. In *SGP* (2006), pp. 227–230.

[CK03] CHOI K.-J., KO H.-S.: Extending the immediate buckling model to triangular meshes for simulating complex clothes. In *Eurographics 2003 Short Presentations* (2003), pp. 187–191.

[dC92] DO CARMO M.: *Riemannian Geometry*. Mathematics: Theory and Applications. Birkhäuser, 1992.

[GGRZ06] GRINSPUN E., GINGOLD Y., REISMAN J., ZORIN D.: Computing discrete shape operators on general meshes. *Comput. Graph. Forum 25*, 3 (2006).

[GHDS03] GRINSPUN E., HIRANI A. N., DESBRUN M., SCHRÖDER P.: Discrete shells. *SCA* (2003), 62–67.

[GSH*04] GINGOLD Y., SECORD A., HAN J. Y., GRINSPUN E., ZORIN D.: *A Discrete Model for Inelastic Deformation of Thin Shells*. Tech. rep., Aug 2004.

[Hau04] HAUTH M.: *Visual Simulation of Deformable Models*. PhD thesis, University of Tübingen, 2004.

[HLW06] HAIRER E., LUBICH C., WANNER G.: *Geometric Numerical Integration: Structure-Preserving Algorithms for Ordinary Differential Equations*. Springer, 2006.

[HP04] HILDEBRANDT K., POLTHIER K.: Anisotropic filtering of non-linear surface features. *CGF 23*, 3 (2004), 391–400.

[Kaw80] KAWABATA S.: *The Standardization and Analysis of Hand Evaluation*. The Hand Evaluation and Standardization Committee, The Textile Machinery Society of Japan, 1980.

[MBF04] MOLINO N., BAO Z., FEDKIW R.: A virtual node algorithm for changing mesh topology during simulation. In *SIGGRAPH* (2004), pp. 385–392.

[Mor99] MORINI B.: Convergence behaviour of inexact newton methods. *Math. of Comp. 68*, 228 (1999), 1605–1613.

[OH99] O'BRIEN J. F., HODGINS J. K.: Graphical modeling and animation of brittle fracture. In *SIGGRAPH* (1999), pp. 137–146.

© Association for Computing Machinery, Inc. 2007.

[PTVF92] PRESS W. H., TEUKOLSKY S. A., VETTERLING W. T., FLANNERY B. P.: *Numerical Recipes in C: The Art of Scientific Computing*. Cam. Univ. Press, 1992.

[SM02] SIDABRAITE V., MASTEIKAITE V.: A preliminary study for evaluation of skirt asymmetric drape. *International Journal of Clothing Science and Technology 14*, 5 (2002), 286–298.

[TF88] TERZOPOULOS D., FLEISCHER K.: Modeling inelastic deformation: Viscoelasticity, plasticity, fracture. In *SIGGRAPH* (1988), pp. 269–278.

[TW06] THOMASZEWSKI B., WACKER M.: Bending Models for Thin Flexible Objects. In *WSCG Short Comm.* (2006).

[VK01] VENTSEL E., KRAUTHAMMER T.: *Thin Plates and Shells*. CRC Press, 2001.

[VMT06] VOLINO P., MAGNENAT-THALMANN N.: Simple linear bending stiffness in particle systems. In *SCA* (2006), pp. 101–106.

[WBH*] WARDETZKY M., BERGOU M., HARMON D., ZORIN D., GRINSPUN E.: Discrete Quadratic Curvature Energies. To appear in CAGD, 2007.

[ZT89] ZIENKIEWICZ O. C., TAYLOR R. L.: *The finite element method*. McGraw Hill, 1989.

Appendix A: Neglected term in force Jacobian

As discussed in §6, we advocate the use of an inexact Newton's method, using only the constant portion of the force Jacobian given in §5. Indeed, for optimal performance (and no loss of accuracy) one should omit calculation of the linear component arising from the nonflat undeformed configuration. However, for completeness of presentation, we include the expression for this linear component below.

With respect to the local position vector $(\mathbf{x}_0, \mathbf{x}_1, \mathbf{x}_2, \mathbf{x}_3) \in \mathbb{R}^{12}$, and the corresponding local force vector $\mathbf{f} = (\mathbf{f}_0, \mathbf{f}_1, \mathbf{f}_2, \mathbf{f}_3) \in \mathbb{R}^{12}$, the local force Jacobian ($\mathbb{R}^{12} \times \mathbb{R}^{12}$) is given by

$$\bar{k} \begin{pmatrix} 0 & (\mathbf{e}_1 - \mathbf{e}_2)^* & (\mathbf{e}_2 - \mathbf{e}_0)^* & (\mathbf{e}_0 - \mathbf{e}_1)^* \\ -(\mathbf{e}_1 - \mathbf{e}_2)^* & 0 & -\mathbf{e}_2^* & \mathbf{e}_1^* \\ -(\mathbf{e}_2 - \mathbf{e}_0)^* & \mathbf{e}_2^* & 0 & -\mathbf{e}_0^* \\ -(\mathbf{e}_0 - \mathbf{e}_1)^* & -\mathbf{e}_1^* & \mathbf{e}_0^* & 0 \end{pmatrix},$$

where each entry represents a 3×3 skew-symmetric subblock; the asterisk applied to a vector, $\mathbf{v}^*$, produces the matrix

$$\mathbf{v}^* = \begin{pmatrix} 0 & -\mathbf{v}_z & \mathbf{v}_y \\ \mathbf{v}_z & 0 & -\mathbf{v}_x \\ -\mathbf{v}_y & \mathbf{v}_x & 0 \end{pmatrix},$$

corresponding to the cross product operation $\mathbf{v} \times (\cdot)$. The local force Jacobian is assembled into the global $\mathbb{R}^{3n} \times \mathbb{R}^{3n}$ Jacobian in the usual manner. While it is most easily expressed by a skew-symmetric matrix of skew-symmetric subblocks, note that $\operatorname{Hess} G(\mathbf{e}_0)$ is indeed symmetric.

Appendix B: Implementing fracture

The material fractures when internal strain exceeds a threshold. For simplicity we only consider fracture along existing mesh edges; however, this limitation can be easily removed, see *e.g.*, [OH99, MBF04, GSH*04]. A hinge edge, $\mathbf{e}_i$, fractures if the bending strain, $\frac{|\mathbf{e}_i|}{A_i}(\theta_i - \bar{\theta}_i)$, exceeds a material-dependent threshold.

Fracture may be viewed as the transition when an interior edge becomes a boundary edge. A mesh edge has one of three states: INTERIOR⟶FRACTURED-INTERIOR⟶BOUNDARY, where the arrows indicate allowable state transitions. An INTERIOR edge becomes FRACTURED-INTERIOR if the strain threshold is exceeded; a FRACTURED-INTERIOR edge becomes BOUNDARY only as a consequence of explicit changes to mesh connectivity, as explained below.

A BOUNDARY vertex is a vertex incident on a FRACTURED-INTERIOR or BOUNDARY edge. A FRACTURED-INTERIOR edge, e_i, may be in one of three configurations, distinguished by the number of incident BOUNDARY vertices:

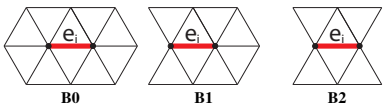

In each case, any BOUNDARY vertices incident on e_i are split into two. Specifically, in case: (**B0**), no action is taken; (**B1**) and (**B2**), one and two vertices are split, respectively, and the resulting change to mesh connectivity causes at least one edge (e_i) but possibly other incident edges to transition FRACTURED-INTERIOR⟶BOUNDARY.

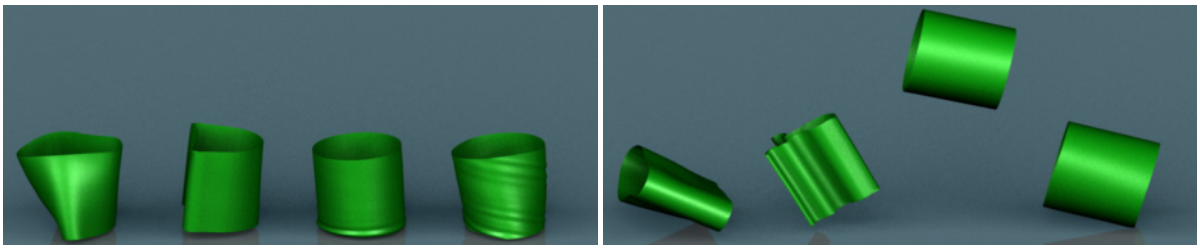

Figure 3: *Thin-shell simulation of falling orthotropic cylinders. Material axes vary from left-to-right: isotropic, vertical, horizontal, diagonal. Left Image: stress formed on the cylinders upon impact. Right Image: the effects of anisotropy after impact. Note the extreme flatenning of the cylinder with axis aligned vertically and the high bounce of the cylinder with axis aligned horizontally.*

Figure 4: *Shear vs. no bending shear: a high bending shear modulus tends to align folds and wrinkles to the material axes (leftmost); a lower shear modulus allows the fabric to fold along other directions, and therefore to obtain a closer fit to the body (second frame). Shearing effects cannot be reproduced by simply tuning Young moduli (3 unsuccessful attempts shown on the right).*

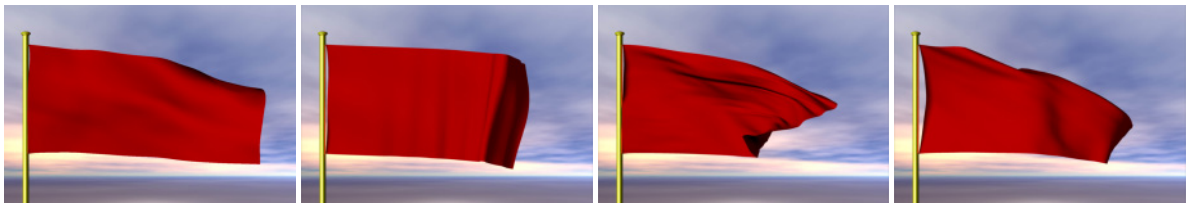

Figure 5: *Varying material axes at no additional cost. From left-to-right: isotropic, vertical, horizontal and diagonal.*

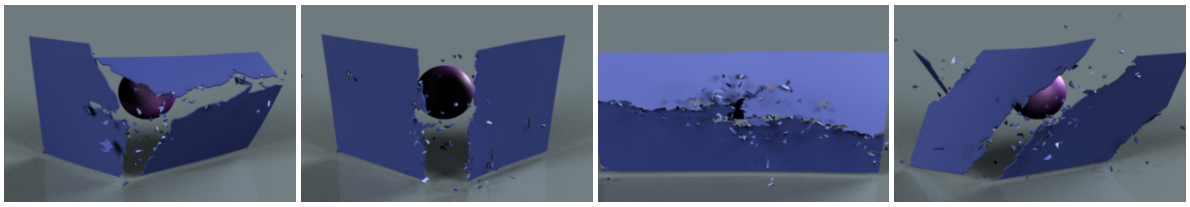

Figure 6: *Thin plates: adjustable directions of fracture patterns. Left-to-right: isotropic, vertical, horizontal and diagonal.*

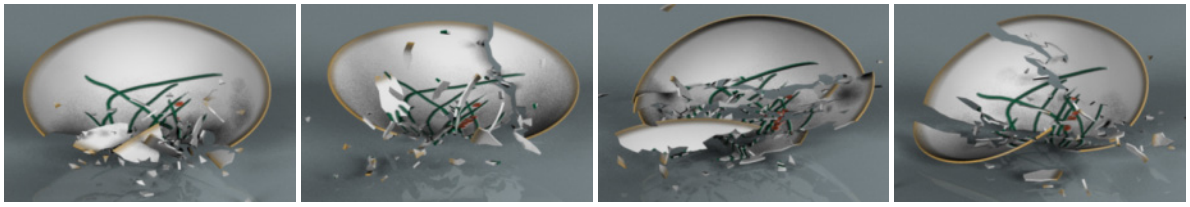

Figure 7: *Thin shells: adjustable directions of fracture patterns. Left-to-right: isotropic, vertical, horizontal and diagonal.*

© Association for Computing Machinery, Inc. 2007.